Influence of phase separation microstructure on the mechanical properties of transparent modifier-free glasses

Zhang, Qi; Jensen, Lars Rosgaard; Youngman, Randall E.; To, Theany; Du, Tao; Bauchy, Mathieu; Smedskjær, Morten Mattrup

Published in:
Journal of Non-Crystalline Solids

DOI (link to publication from Publisher):
10.1016/j.jnoncrysol.2022.121806

Publication date:
2022

Document Version
Publisher's PDF, also known as Version of record

Journal of Non-Crystalline Solids 595 (2022) 121806

Contents lists available at ScienceDirect

Journal of Non-Crystalline Solids

journal homepage: www.elsevier.com/locate/jnoncrysol

Influence of phase separation microstructure on the mechanical properties of transparent modifier-free glasses

Qi Zhang [a], Lars R. Jensen [b], Randall E. Youngman [c], Theany To [a], Tao Du [a], Mathieu Bauchy [d], Morten M. Smedskjaer [a,*]

[a] Department of Chemistry and Bioscience, Aalborg University, Aalborg, Denmark
[b] Department of Materials and Production, Aalborg University, Aalborg, Denmark
[c] Science and Technology Division, Corning Incorporated, Corning, NY, USA
[d] Department of Civil and Environmental Engineering, University of California, Los Angeles, USA

ARTICLE INFO

Keywords:
Oxide glasses
Phase separation
Fracture toughness
Crack resistance
Indentation
Transparency

ABSTRACT

In this work, we use heat treatment to vary the size of nanoscale droplets in a phase-separated B_2O_3-SiO_2-Al_2O_3-P_2O_5 glass without traditional modifiers and explore the effect of phase separation on the mechanical properties. The melt-quenched version of this glass already exhibits phase separation with a droplet phase rich in B_2O_3. The glass transition temperature (T_g) of the droplet phase is lower than that of silica-rich glass matrix. Upon heat treatment at a temperature below the T_g of the droplet phase, the size of droplets decreases but the fraction of the droplet phase increases. Consequently, the crack initiation resistance more than doubles. Upon heat treatment at the T_g of the matrix phase, the fracture toughness increases from 0.61 to 0.73 MPa·m$^{0.5}$, which is primarily due to the aggregation of individual droplets. Upon the different heat treatments, the phase-separated glasses retain their optical transparency, while the hardness increases slightly.

1. Introduction

Oxide glass materials play a critical role in consumer electronics, energy, information technology, and other important industrial areas due to their unique properties, such as optical transparency, high hardness, and properties that are tunable by composition and structure tuning [1,2]. Compared to other optically transparent analogues like polymers and some crystals, glass materials combine good mechanical properties and chemical stability with low cost. Therefore, they are widely used for fiber applications, flexible substrates, roll-to-roll processing of displays, solar modules, planar lighting devices, next-generation touch-screen devices and large-scale architectural glazing, etc. However, their high brittleness is a major bottleneck, which limits the application ranges [1]. To improve the glass mechanical properties, the complex structure of glasses, involving both short- and intermediate-range order, needs to be understood and controlled [2]. The common strategy to improve the mechanical performance of glasses generally involves methods to prohibit (i) the generation of new cracks and/or limit (ii) the growth of pre-existing cracks. The former is typically quantified by indentation as the crack initiation resistance (*CR*), while the latter is evaluated by measuring the fracture toughness (K_{Ic}). The difference between *CR* and K_{Ic} is discussed in details in Ref. [3]. Recently, the design of damage-tolerant glasses based on microstructure optimization has attracted attention as an additional degree of freedom as compared to simple composition optimization or post-processing techniques such as thermal tempering and ion exchange to induce surface compressive stresses [4–6].

So-called extrinsic strengthening techniques typically rely on the use of reinforcements to control the driving force at the crack tip, e.g. through the crack opening displacement and crack-tip shielding [7,8]. In contrast, intrinsic techniques rely on the optimization of the inherent fracture resistance of the glass network by tuning the structure [1]. For example, rigid glasses with fully polymerized networks can exhibit high resistance to crack growth and thus resulting in high K_{Ic} [5,9]. On the other hand, glasses with large free volume or with self-adaptive networks can feature high *CR* since energy dissipation can easily occur through densification process [10,11]. Typical approaches for tailoring the glass microstructure involve liquid-liquid phase separation or partial crystallization to form glass ceramics. For both approaches, the mechanical properties are influenced by the composition, shape, and

* Corresponding author.
E-mail address: mos@bio.aau.dk (M.M. Smedskjaer).

https://doi.org/10.1016/j.jnoncrysol.2022.121806
Received 29 May 2022; Received in revised form 29 June 2022; Accepted 11 July 2022
Available online 4 August 2022

fraction of the secondary phase. For example, Dong et al. found that the formation of $Ba_3Nb_{10}O_{28}$ crystals in a borosilicate glass enhances the crack resistance significantly since the crystalline phase acts as a "crack bridge" [12]. Yang et al. found that the conversion between two different zirconia crystalline phases (tetragonal to monoclinic ZrO_2) in a glass with the composition MgF_2-Al_2O_3-B_2O_3-P_2O_5-MgO-SiO_2-K_2O consumes the fracture energy and thus reduces the driving force for the crack extension [13,14]. However, these reinforcements can cause the glass to lose its unique advantage, i.e., transparency in the visible region [15].

Studies have shown that compliant inclusion droplets within a stiff matrix can attract and arrest cracks by undergoing local failure [16], whereas stiff inclusions can redirect cracks to the interface [16] or promote multiple failures around them [17]. As an example, some phase-separated borosilicate glasses with higher interconnectivity exhibit a 50% increase in their indentation fracture toughness compared to the as-prepared glass without phase separation [18], clearly demonstrating the potential of using phase separation as a toughening mechanism. However, as inclusions larger than ~500 nm typically induce a loss of transparency [19], phase separation with nanometric droplets of well-controlled sizes is required [20,21]. Moreover, the relation between glass microstructure and mechanical properties is not yet well understood [18,22].

The volume fraction and size of the droplet phase in phase-separated glasses are two important factors affecting the mechanical properties [18,22–24]. Furthermore, Cheng et al. have investigated the indentation cracking behavior and its relation to structure in glasses featuring nanophase separation, finding that the droplet boron-rich phase in the silica matrix could restrain the cracks [25]. In general, borosilicate glass has been found to be a good base glass system to induce a soft droplet phase and tune the phase composition through heat treatment [18,26]. However, the separated boron-rich phase is usually formed in glasses with both network modifiers (such as Li^+ or Na^+) and formers, and such borosilicate glasses can suffer from chemical instability, sensitivity to water and be prone to crystallization upon heat treatments [27]. Meanwhile, the relation among phase separation and mechanical properties has not been well studied for network glasses without traditional network modifiers. It is therefore of interest to investigate nanophase separation in borate-based glass without modifiers. Specifically, based on the work of Liu et al. [20], we choose a modifier-free glass (B_2O_3-SiO_2-Al_2O_3-P_2O_5) that is prone to nanoscale phase separation as our glass system, in which alumina plays the role as a network intermediate in the glass. We vary the phase separation process through heat treatments, on the premise of keeping the glass transparent, and then measure three mechanical properties, namely, hardness, crack initiation resistance, and fracture toughness. In addition, the glass structure and phase separation morphology are studied to reveal the relationship between microstructure and mechanical properties.

2. Experimental methods

2.1. Sample preparation

We used the glass of composition $27.7B_2O_3$–$58.4SiO_2$–$3.9Al_2O_3$–$10P_2O_5$ (in mol%) from our previous study [20]. It was prepared by melting the mixture of raw materials (sand, calcined alumina, boric acid, and boron orthophosphate, with 0.14 wt.% SnO added for fining) in Pt crucibles at 1600°C for 6 h in an electrical furnace. Then the melt was quenched by pouring into a water bath. The resulting small glass pieces were then collected and remelted at 1650 °C for 6 h. Finally, the melt was quenched on a stainless-steel plate to obtain bulk glass samples. The obtained glasses were quickly moved to a preheated annealing furnace at an estimated glass transition temperature value (based on the previous studies) for 30 min and cooled down to room temperature [20]. As the phase-separated glass contains two glass transition temperatures, we chose a temperature of 768 K that is between two T_g values as the annealing temperature.

The analyzed composition of the glass given above was determined by inductively coupled plasma optical emission spectroscopy. According to the previous study [20], this glass exhibits droplet-type phase separation with a droplet glass phase (termed G1) and a matrix glass phase (G2), with corresponding calorimetric glass transition temperatures of T_{g1} = 694 K and T_{g2} = 892 K, respectively. In this study, we further heat-treated the melt-quenched glass for 4 h at different temperatures around these values (648 K, 790 K, and 892 K) to explore the effect of heat treatment on glass atomic-scale and micro-scale structure as well as the mechanical properties and optical transparency. We did not perform heat treatment at temperatures above T_{g2} to avoid any crystallization. In order to control the heat treatment duration and release stress, glass samples were quickly raised to the desired temperature and allowed to furnace cool after holding at the desired temperature. All glass samples in this paper come from the same melt.

2.2. Structural characterization

To confirm that the glass samples did not crystallize upon heat treatment, we characterized the samples by X-ray diffraction (XRD) analysis (Empyrean XRD, PANalytical) with a monochromator Cu Kα radiation (1.5406 Å). Spectra were acquired in the range from 10° to 70° at 40 kV with a scanning speed of $8°min^{-1}$.

The phase morphology of the studied glasses was investigated with a field emission scanning electron microscope (SEM) (Zeiss Cross Beam) at an acceleration voltage of 10 kV. Prior to the SEM measurements, we etched the polished samples in 10% HF for 10 min to improve the contrast between the droplet and matrix glass phases. All samples were gold coated before testing. The size distribution of the droplet phase was analyzed based on the SEM images using the ImageJ software. The droplet area was measured and the average diameter of the droplet was calculated. The software operation method details can be found in Refs. [28–30].

To study if any changes in the short-range order structure of the B, Al, and P network formers occurred upon heat treatment, we performed solid-state nuclear magnetic resonance (NMR) spectroscopy. ^{11}B and ^{27}Al magic-angle spinning (MAS) NMR spectra were recorded on an Agilent DD2 spectrometer with a 3.2 mm MAS NMR probe at a magnetic field of 16.4 T. Powdered glass samples were packed into 3.2 mm outer diameter zirconia rotors and spun at 20 and 22 kHz for ^{11}B and ^{27}Al MAS NMR, respectively. The data were collected at resonance frequencies of 224.5 and 182.3 MHz for ^{11}B and ^{27}Al, respectively, while a short radiofrequency (rf) pulse of 0.6 μs (π/12 tip angle) was used with a recycle delay of 5 s and 2 s for ^{11}B and ^{27}Al, respectively. Signal averaging was performed using 600 to 1000 scans for each sample. ^{31}P MAS NMR spectra were recorded on a Varian VNMRs spectrometer and a 3.2 mm MAS NMR probe at a magnetic field of 11.7 T with 202.3 MHz resonance frequency. Powdered glass samples were contained in 3.2 mm outer diameter zirconia rotors and spun at 20 kHz. The signal averaging for ^{31}P was performed with 400–800 scans using a short rf pulse of 1.2 μs (π/6 tip angle) and a recycle delay of 120 s. All NMR data were processed without any additional line broadening. The data were plotted using the normal shielding convention, while the frequency of ^{11}B, ^{27}Al, and ^{31}P NMR data were referenced to aqueous boric acid (19.6 ppm), aqueous aluminum nitrate (0.0 ppm) and 85% H_3PO_4 solution (0.0 ppm), respectively. The ^{11}B and ^{27}Al MAS NMR data were fit using DMFit software with second-order quadrupolar lineshapes for the 3-fold coordinated boron peaks and a combination of Gaussian and Lorentzian lineshapes for the 4-fold coordinated peaks, while the CzSimple lineshape model was used for ^{27}Al. The ^{31}P MAS NMR data were also fit using DMFit but with 100% Gaussian lineshapes [31,32].

To obtain further structural information also at the medium-range length scale, we acquired micro-Raman spectra (inVia, Renishaw) of the studied glass surfaces in the 120–1600 cm^{-1} wavenumber range. Measurements were done using a 532 nm diode pumped solid state laser

for an acquisition time of 10 s. Spectra from five different surface locations were collected to ensure homogeneity. All spectra were uniformly treated in Origin software for background correction and area normalization.

2.3. Property characterization

The glass transition temperatures (T_g) of the phase-separated glasses were determined using differential scanning calorimetry (DSC) (STA 449 F1, Netzsch). We used samples polished down to a thickness of 1 mm. These were tested in Pt crucibles under a flow of argon (gas flow 60 mL·min^{-1}). The heating rate and the prior cooling rate were both 10 K·min^{-1}. The intercept between the tangent to the inflection point of the endothermic peak and the extrapolated heat flow of the glass was interpreted as the T_g of each phase, i.e., the droplet and matrix glass phases. The error in the determined T_g value is around ±5 K.

Vickers hardness (H_V) and crack resistance (CR) of the samples were determined by using a Nanovea CB500 hardness tester. The glass specimens were successively polished by SiC paper with decreasing abrasive particle size (up to grit 4000) in ethanol and finally with a water-free 1 μm diamond suspension. The indentations were performed using a Vickers indenter tip (four-sided pyramid-shaped diamond with an angle of 136°). To determine H_V, 20 indents were performed for each specimen at a load of 4.9 N applied for 10 s, which was low enough to ensure that no cracks formed upon the indentation at this load. The H_V values were calculated as $H_V = 1.8544P/d^2$, where P is the contact load and d is the average length of the indent diagonals [33]. CR was also determined by using Vickers indentation, but by applying different loads. Each glass specimen was indented 30 times per load, increasing in steps from 0.1 N to 19 N with loading duration of 15 s and dwell time of 10 s, while the loading/unloading rate value was 50 N·min^{-1}. Following indentation, the number of corner cracks was counted. According to the method of Wada et al. [34], the probability of crack initiation is defined as the ratio between the number of corners with cracks and the total number of corners on all indents (i.e., four corners for Vickers indenter). CR was determined as the load at which the crack probability is 50%. All indentations were conducted at room temperature (~295 K) and relative humidity of 25–32%.

Fracture toughness (K_{Ic}) was determined using the single-edge precrack beam (SEPB) method, following the well-established procedure [35,36]. First, four pieces of glass were cut from the annealed glass bulk, and three of them were heat-treated under different heat treatment conditions. Each of the four samples were cut into five glass beams with dimension of 1.5 × 2 × 10 mm^3 and then polished. Then eight Vickers indents with a load of 9.8 N for a dwell time of 5 s were placed on a line on the breadth side (B = 1.5 mm). The indented specimen was positioned in a compression fixture with a groove size of approximately 3 mm (1.5 times the specimen width, W = 2 mm) to produce a precrack with a cross-head speed of 0.05 mm·min^{-1}. Under the compression fixture, the lower part of the specimen (indented or grooved part) experienced tensile stress, whereas the upper part experienced compressive stress. The tensile stress opened a crack from the indent corners and allowed it to propagate until it reached the compressive stress region (approximately at the middle of the specimen width). This prevented further extension of the precrack and allowed us to obtain a precrack with the size about half-length of W. Then, the precracked specimen was positioned in a three-point bending fixture and the specimen was fractured with a cross-head speed of 10 μm·s^{-1} to avoid humidity effects [36,37]. We note that this adapted three-point bending span (S) of 7.5 mm was designed to fulfill the span-to-width ratio of about 4 as required in the standard [38]. K_{Ic} was then calculated from the peak load (P_{max}) [36,37],

$$K_{Ic} = \frac{P_{max}}{B\sqrt{W}}Y^*,$$

Where

$$Y^* = \frac{3}{2}\frac{S}{W}\frac{\alpha^{1/2}}{(1-\alpha)^{3/2}}f(\alpha) \quad (1)$$

where α is the precrack-width ratio (a/W) and $f(\alpha) = [1.99 - (\alpha - \alpha^2)(2.15 - 3.93\alpha + 2.7\alpha^2)]/(1 + 2\alpha)$. The average K_{Ic} value was calculated from the results of five valid tests.

An example of fracture toughness measurement is shown in Fig. 1. Fig. 1a shows the typical load-displacement curves of the indented glasses. An indented glass specimen was placed into the bridge-compressive fixture (see inset of Fig. 1a) and it was ensured that the indentation line was in the middle of the groove. Under the bridge-compressive fixture, the tensile stress from the groove part opened up the crack from the indentation line, and the length of the produced precrack was around 50% of the specimen width. The precracked specimen was placed into the three-point bending fixture and it was ensured that the precrack was in the middle, as shown in Fig. 1b. Fig. 1b also shows a typical load-displacement curves of a precracked glass. The P_{max} value can be obtained from the load-displacement curve. Finally, the precrack length of the fractured specimen was measured by magnification microscope (Fig. 1c). The details of the experimental setup and testing can be found in Ref. [35].

To investigate the effect of heat treatment and thus phase separation microstructure on the optical transparency of the glass sample, we used an ultraviolet-visible (UV–VIS) spectrometer (Cary 50 Bio, Varian) to determine the optical transparency of 2.0 mm thick polished glass sample. The wavelength range of transmission spectrum was set to 200–800 nm. The average transmittance was calculated from the results of three specimens for each glass sample. All the UV–VIS transmittance spectra were normalized to a thickness of 1 mm.

3. Results

3.1. Phase microstructure analysis

As shown in Fig. 2a, the phase-separated glasses remain non-crystalline upon the different heat treatments, as no sharp diffraction peaks are observed. In the previous work, it was suggested that the studied glass exhibits two distinct glass transition temperatures, i.e., the lower T_{g1} corresponding to the droplet phase (rich in B_2O_3) and the higher T_{g2} corresponding to the glass matrix phase (rich in B-O-Si linkages) [20]. Fig. 2b shows the DSC heating curves of the as-prepared and heat-treated glasses. Indeed, we observe two well-separated glass transition peaks in all samples, confirming that the glasses remain phase-separated after heat treatments. For the glass heat-treated at 648 K, T_{g1} decreases from 694 K (for the as-prepared glass) of the as-prepared glass to 677 K, while T_{g2} slightly increases from 892 K to 900 K. Considering the error in T_g determination being ±5 K, the T_{g2} values of glass heat-treated at 648 K are within the measurement error. As such, T_{g1} is trending toward the T_g value of vitreous B_2O_3 (around 533 K), but still significantly above, showing that the droplet phase is not made of pure B_2O_3 (see more details later). For the glasses heat-treated at 790 K and 892 K, T_{g1} decreases slightly to around 685 K but also within the measurement error. T_{g2} of the glass heat-treated at 790 K decreases significantly to 843 K, while for the glass heat-treated at 892 K, T_{g2} decrease to 879 K. In conclusion, the heat treatment below T_{g1} mainly influences the separated phase, and heat treatment above T_{g1} mainly affects the glass matrix phase. The details are shown in Figure S1.

To explore the changes in the microstructure of the phase-separated glasses after heat treatment, we performed SEM measurements on the glass surfaces after etching treatment. Fig. 3 shows the morphology and size distribution of the droplet phase in these etched samples. Spherical phases but with different sizes are present in all samples. In the study of Liu et al. on the same glasses, the droplet phase could be identified to be one rich in B_2O_3, including boroxol rings [20]. Here, we find for the

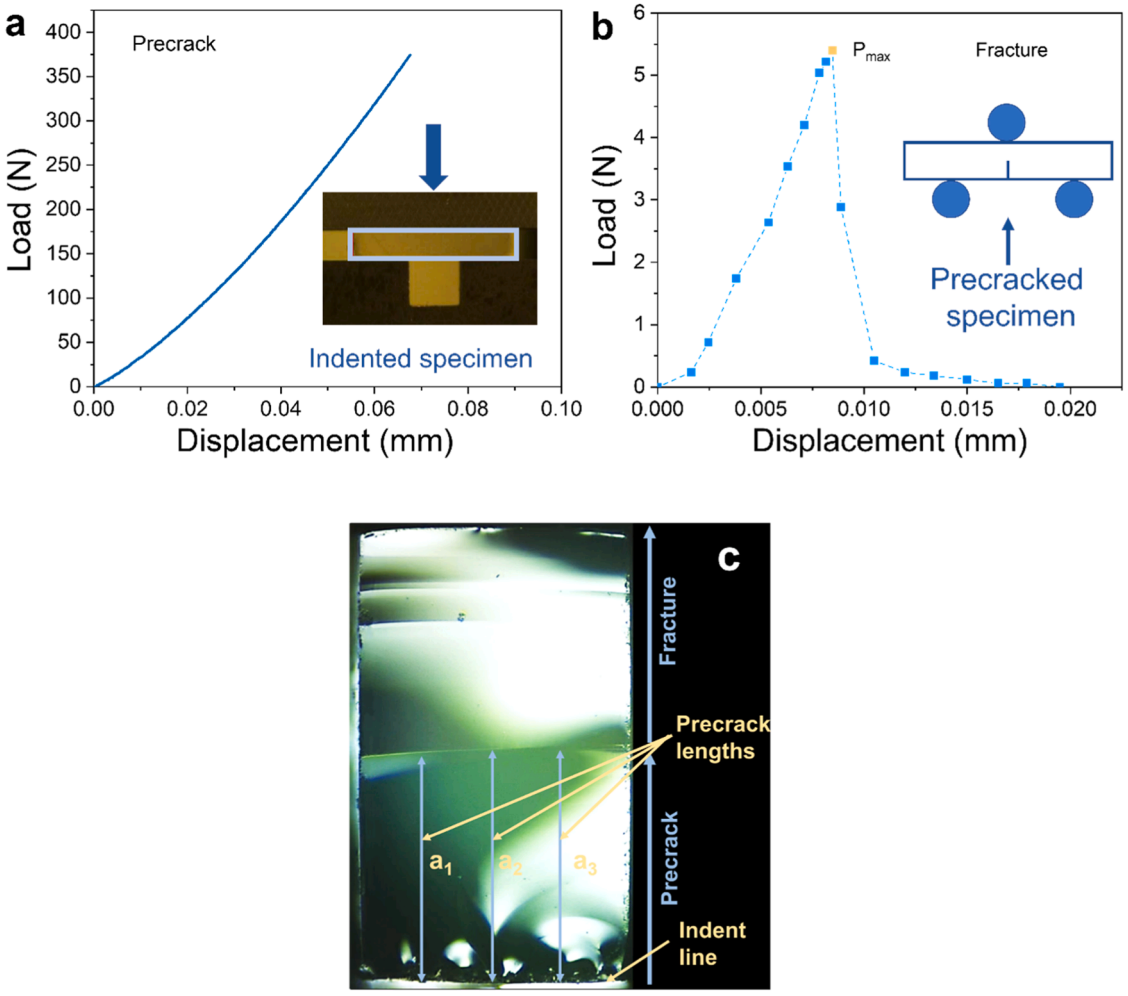

Fig. 1. Fracture toughness measurement. (a) Load−displacement curves of a glass specimen. The inset shows the bridge-compression fixture as captured during precracking. (b) Load-displacement curves of three-point bending of the precracked SEPB specimens. The three-point bending fixture with a precracked specimen is shown in the inset. (c) Post-fractured SEPB specimen.

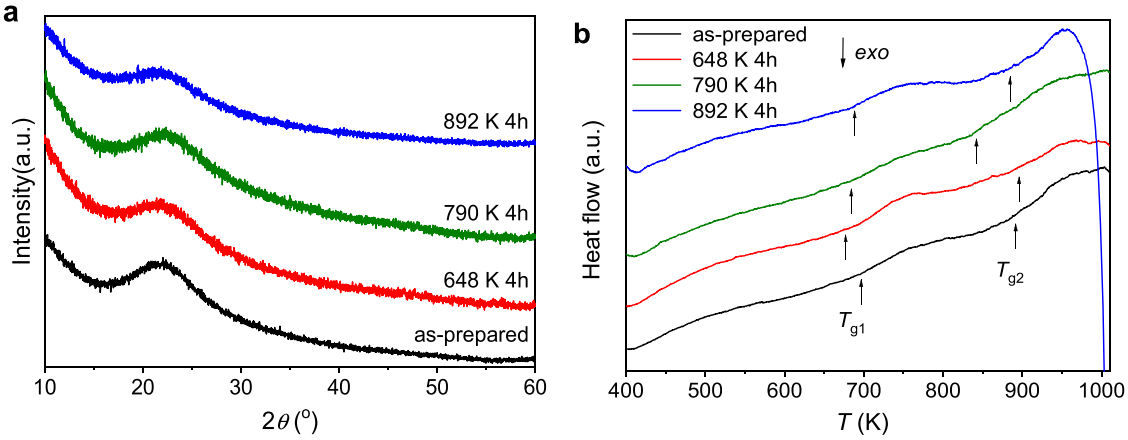

Fig. 2. (a) XRD patterns and (b) DSC heating curves (at 10 K·min^{-1}) of as-prepared glass and glass samples heat-treated at 648 K for 4 h, 790 K for 4 h, and 892 K for 4 h. The two arrows in each curve indicate the onset temperature of the endothermic glass transitions of the droplet and matrix phases in each sample, respectively.

as-prepared glass that the average size of the droplet phase is around 87 nm, while it decreases to 63 nm upon heat treatment at 648 K. As the heat treatment temperature further increases to 790 K, the average size of the droplet continues to decrease to 57 nm. When the temperature increases to 892 K, the average size of the single droplet phase is about 77 nm, but we note some agglomeration of the droplets (see inset in Figs. 3d and S2), which can reach a size of more than 300 nm. The average size of the droplets is listed in Table 1.

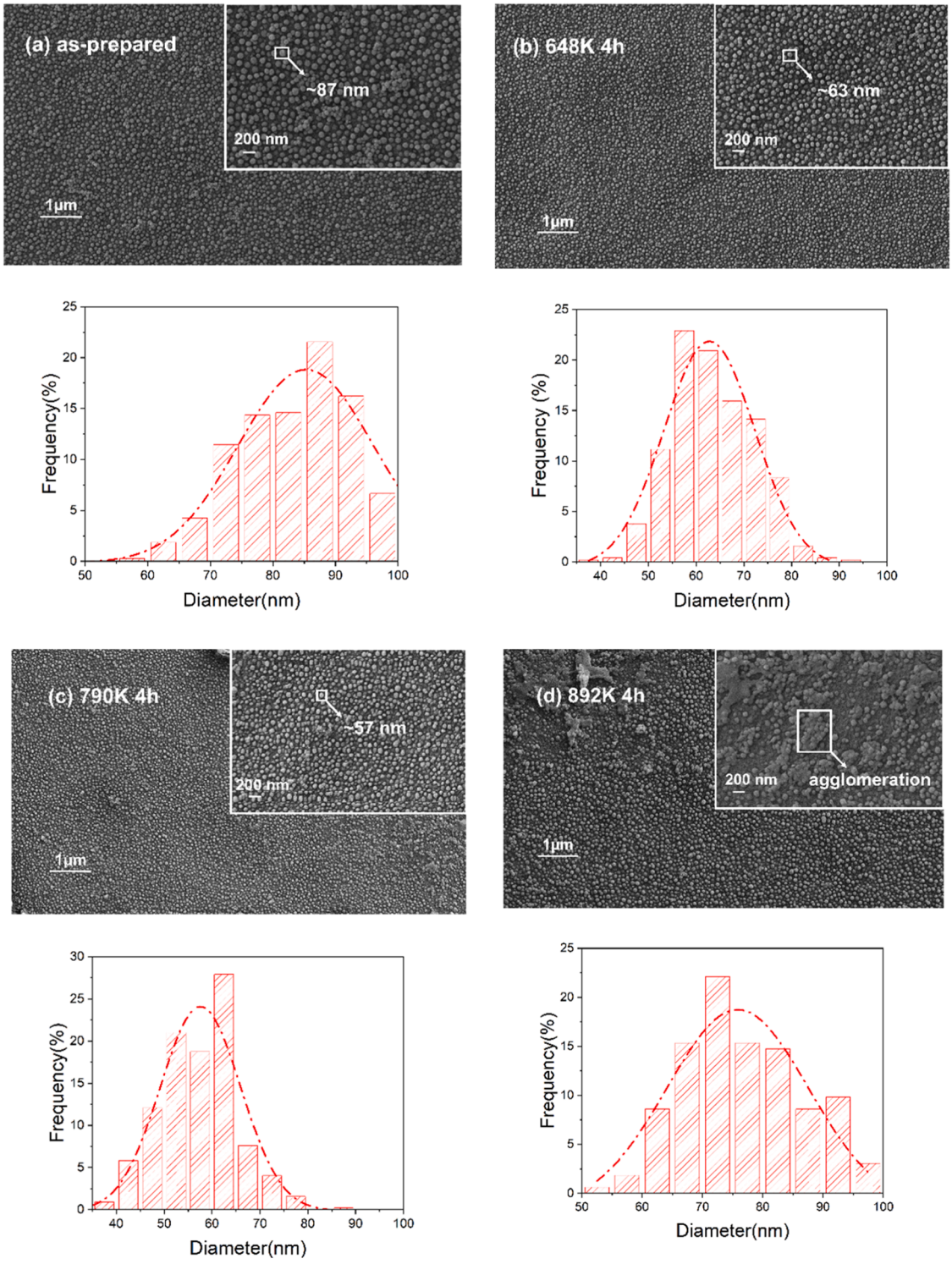

Fig. 3. SEM micrographs and droplet phase size distribution in the different glass samples before and after heat treatments: (a) as-prepared glass, (b) 648 K for 4 h, (c) 790 K for 4 h, and (d) 892 K for 4 h.

3.2. Glass network structure

Fig. 4 shows the Raman spectra of the studied glasses in the frequency range of 200–1500 cm^{-1}, and the enlarged view around 800 cm^{-1} is shown in Fig. S3. Each spectrum consists of six bands or band regions, which are centered at ~465 cm^{-1}, ~715 cm^{-1}, ~805 cm^{-1}, ~935 cm^{-1}, ~1145 cm^{-1} and ~1315 cm^{-1}, respectively. The band situated at 200 to 620 cm^{-1} can be attributed to mixed bending and stretching vibrations of the bridging oxygens (BOs) [39–42], while the band centered at ~1145 cm^{-1} can be assigned to Q^4 units of Si (SiO_4 tetrahedra with 4 BOs) [43]. The relative intensity of these two bands increases upon heat treatment, indicating an increased connectivity of the glass structure. The Raman band at ~805 cm^{-1} is associated with the breathing vibration of boroxol rings [11,44], and its intensity increases upon heat treatment at 648 K, whereas it decreases for the glass heat-treated at 892 K. For the glass heat-treated at 790 K, the intensity of

Table 1
Droplet average size, Vickers hardness at 4.9 N (H_V), crack resistance (CR), and fracture toughness (K_{Ic}) measured using the SEPB technique of the as-prepared and heat-treated glasses.

Sample ID	Droplet Average Size [nm]	H_V [GPa]	CR [N]	K_{Ic} [MPa·m$^{0.5}$]
as-prepared	87	4.9 ± 0.1	5.2 ± 0.1	0.61 ± 0.02
648 K 4h	63	5.5 ± 0.2	11.2 ± 0.2	0.69 ± 0.03
790 K 4h	57	5.3 ± 0.1	8.7 ± 0.2	0.65 ± 0.03
892 K 4h	77	5.3 ± 0.1	7.7 ± 0.1	0.73 ± 0.02

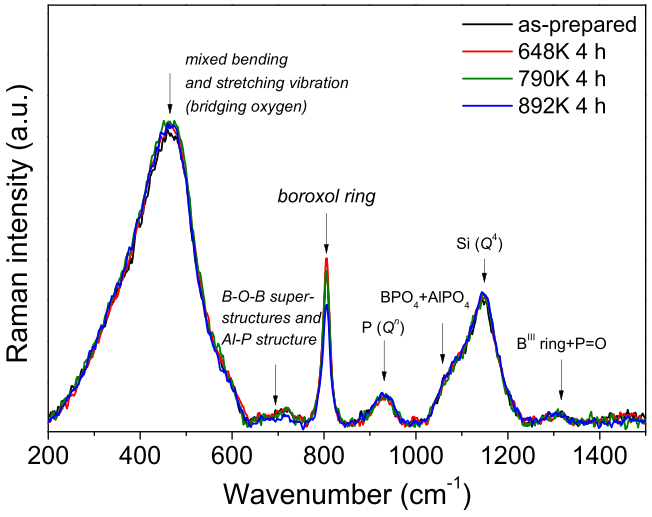

Fig. 4. Raman spectra of as-prepared glass and glass samples heat-treated at 648 K for 4 h, 790 K for 4 h, and 892 K for 4 h.

boroxol ring band is only slightly increased. This indicates that the higher treatment temperature (around T_{g2}) induces the boroxol ring structure to partially transform to other borates structure, while the lower heat treatment temperature (below T_{g1}) facilitates more droplet phase formation. The other bands, which are located at ~715 cm^{-1}, ~935 cm^{-1}, ~1315 cm^{-1}, and a shoulder at ~1080 cm^{-1} can be assigned to B-O-B superstructural unit and Al-P structure, P (Q^4), B^{III} ring and $P{=}O$, and BPO_4^-, and $AlPO_4^-$, respectively. The intensity of these bands does not change significantly upon heat treatments.

Fig. 5 shows the ^{11}B, ^{27}Al, and ^{31}P MAS NMR spectra of the four studied glass samples. Fig. 5a and 5b show the normalized ^{11}B MAS NMR spectra and deconvolution of the spectrum for the as-prepared glass, respectively. The deconvolution results of boron speciation for the entire series are shown in Table 2, and the deconvoluted ^{11}B MAS NMR spectra of each glass are shown in Fig. S4. The peaks centered near −4 ppm correspond to [BO_4], while the broad signal between 2 and 20 ppm corresponds to [BO_3] structural units. From the deconvolution, we calculate the fraction of tetrahedral to total boron (N_4). Upon heat treatment, N_4 increases from 18.3% in the as-prepared glass to 18.6% in the glass heat-treated at 892 K, i.e., a very small change in boron speciation. After deconvolution, [BO_3] structural units can be separated into three resonances, and the peak having an isotropic chemical shift of 17.4 ppm is assigned to ring B^{III}. Thus, we also find that the fraction of ring B^{III} increases from 19.3% in the as-prepared glass to 19.9% in the glass after heat treatment at 648 K, which could be related to an increase in the fraction of droplet phase (rich in B_2O_3 and boroxol ring structure) upon this heat treatment. We here note that the uncertainties in N_4 values (see Table 2) are determined from fitting of the MAS NMR data and consideration of the overlapping satellite transition spinning sidebands. While the uncertainty is larger than the differences between some of the glasses, the relative changes in NMR lineshape and thus N_4 values, are significantly more precise. That is, even a small difference in N_4 is meaningful given the identical way N_4 is determined, as indicated by subtle changes in peak intensities in Fig. 5a.

Considering the ^{31}P MAS NMR spectra (Fig. 5c), the peak centered at −33.7 ppm corresponds to the resonance of P Q^4 (PO_4 tetrahedra with 4 BOs) bonded to Al ($AlPO_4$-like units) and B (BPO_4-like units). This band exhibits only negligible changes upon heat treatment, i.e., the heat treatments have no significant effect on the phosphorus speciation. We note that based on the NMR line shapes, there is no evidence for any small $AlPO_4$ or BPO_4 crystallites. This confirms that both the as-prepared and heat-treated glasses are non-crystalline, as consistent with the XRD results. We also note that the observation of only P Q^4 groups indicates that the glasses do not contain any non-bridging oxygens.

The ^{27}Al MAS NMR spectra (Fig. 5d) can be deconvoluted into three Al resonances, centered around 38, 6, and −19 ppm, corresponding to Al^{IV}, Al^{V}, and Al^{VI}, respectively. The deconvoluted ^{27}Al MAS NMR spectra are shown in Fig. S5, and the derived aluminum speciation results are shown in Table S1. These resonances are all shifted to higher shielding than those usually observed in aluminosilicate glasses due to the existence of P as the next-nearest neighbor (NNN) aluminum polyhedra and the higher electronegativity of P compared to that of Si [20, 45]. The NMR shifts of these three resonances are all consistent with substantial Al-O-P bonding (i.e., all have P NNN) [20]. Upon heat treatment, the fraction of Al^{V} decreases from 16% in the as-prepared glass to 15% in the heat-treated samples. Meanwhile, the fraction of Al^{VI} also decreases upon heat treatment from 3% in the as-prepared glass to 2% in the glass heat-treated at 648 K and 892 K, and to 1% in the glass heat-treated at 790 K. The average coordination number of aluminum is slightly decreased from 4.22 of as-prepared glass to 4.17 of glass heat treated at 790 K. For the glass heat-treated at 648 K and 892 K, the average coordination number of aluminum is around 4.19, which is also slightly lower than that of the as-prepared glass. According to the previous research in this modifier-free glass system [20], Al^{V} and Al^{VI} units are present as charge-balancing polyhedra, and Al^{IV} combines with P *NNN* to form $AlPO_4$-like units. In this modifier-free glass, the Si-O network consists of structural Si Q^4 units, i.e., with four bridging oxygens bonded to Si. In addition, other glass formers also form different structural units, such as P Q^4, [BO_3], and [BO_4]. As glass intermediate, portions of Al^{3+} bonded with four bridging oxygen to form Al^{IV} also join into the glass network. Due to the lack of any traditional modifiers in the studied glass, the non-network forming fraction of Al^{3+}act as the only cation to balance the charges of various structural units in the glass network, resulting in the formation of Al^{V} and Al^{VI} units in the glass.

It has been reported that when the B_2O_3 content increases, the fraction of droplet phase increases, meanwhile the average coordination number of aluminum slightly decreases [20]. The main structure of droplet phase might be boroxol ring (B_3O_6), which only contains BOs [46]. Since the P-related structure does not exhibit any changes upon heat treatment (Fig. 5c), the main network structure of the glass matrix phase we consider here is the Si-O-B network [20]. After heat-treatment, the reduced size of droplet phase will lead to an increased interface area between droplet phase and glass matrix, so the glass heat-treated at 790 K with the smallest average size of droplet exhibits the lowest average coordination number of aluminum. Secondly, the increase in the fraction of droplet phase contributes to the formation of B-O-B, which would also decrease the average coordination number of aluminum. The latter is also confirmed by the Raman results (Fig. 4). Finally, the observed decrease in the fraction of Al^{V} and Al^{VI} reflected through the ^{27}Al MAS NMR data (Fig. 5d) could be because the heat treatment enables a small amount of P to move from droplet to matrix phase. This extra P is then available to be coordinated with tetrahedral Al in the form of $AlPO_4$-like groups, which then removes some of the higher coordinated Al polyhedra.

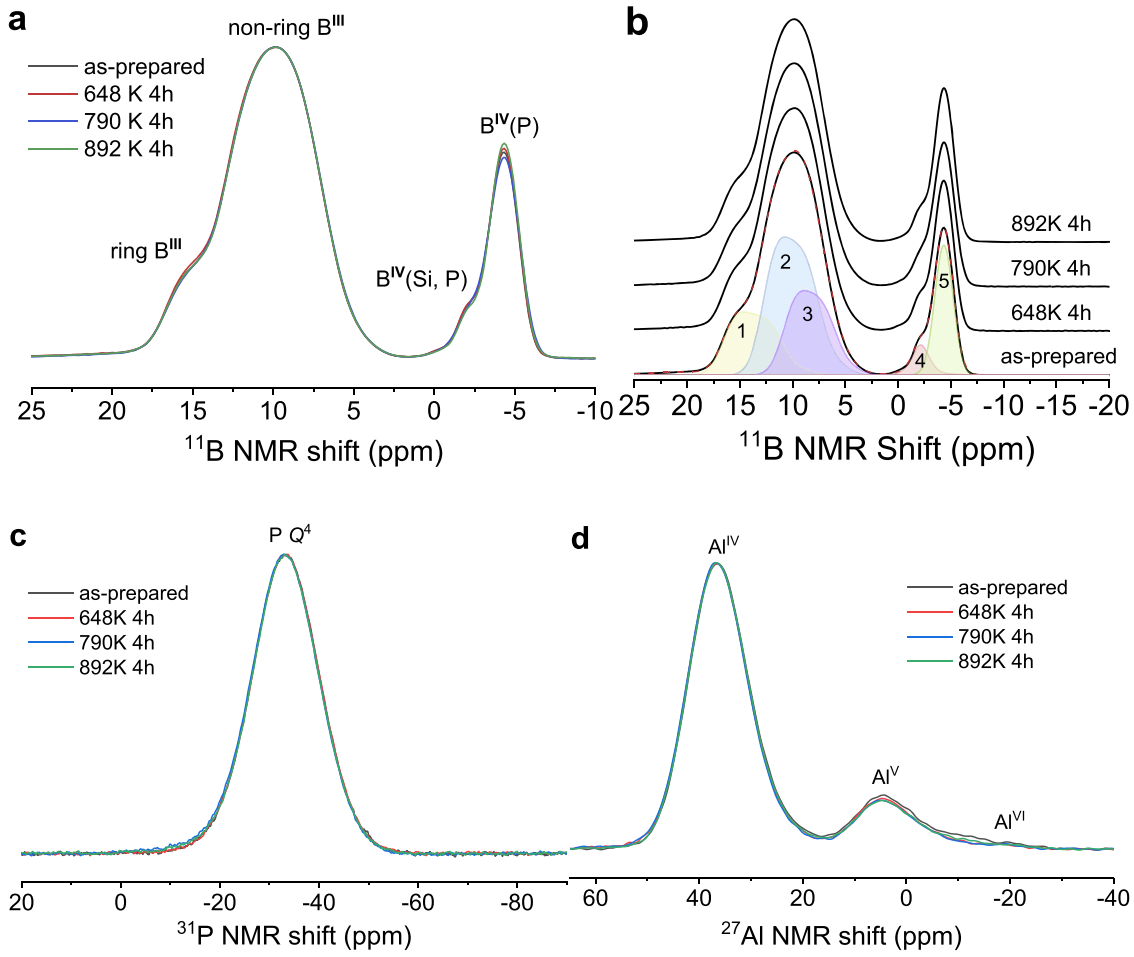

Fig. 5. MAS NMR spectra of the studied glasses: (a) ^{11}B, (b) deconvoluted ^{11}B spectra of as-prepared glass, (c) ^{31}P, (d) ^{27}Al.

Table 2
Boron speciation from ^{11}B MAS NMR spectra deconvolution (Figs. 5b and S4). The uncertainties for the isotropic chemical shift and area fraction of the B^{III} resonances are ± 0.5 ppm and 0.5%, while errors for shift and area fraction for the B^{IV} resonances do not exceed ± 0.1 ppm and ± 0.2%. The uncertainty in N_4 is on the order of ± 0.2%.

Sample ID	1-B^{III} (ring)		2-B^{III} (non-ring)		3-B^{III}		4-B^{IV}		5-B^{IV}		N4
	Shift (ppm)	Area (%)	shift (ppm)	Area (%)	Shift (ppm)	Area (%)	shift (ppm)	Area (%)	shift (ppm)	Area (%)	(%)
as-prepared	17.4	19.3	13.5	39.8	11.5	22.6	−2.2	3.8	−4.4	14.5	18.3
648 K 4h	17.4	19.9	13.5	39.0	11.5	22.6	−2.1	3.9	−4.4	14.6	18.5
790 K 4h	17.4	19.4	13.5	38.7	11.5	23.3	−2.2	4.1	−4.4	14.5	18.6
892 K 4h	17.4	19.3	13.5	39.2	11.5	22.9	−2.1	3.5	−4.4	15.1	18.6

3.3. Mechanical properties

The mechanical properties of the as-prepared and heat-treated glasses are summarized in Table 1, including Vickers hardness, crack resistance, and fracture toughness measured using the SEPB technique. First, we find that the hardness increases from 4.9 GPa for the as-prepared glass to about 5.3 to 5.5 GPa for the heat-treated samples, i.e., the hardness increases slightly with heat treatment. Compared with the fracture toughness (K_{Ic}) value of 0.61 MPa·m$^{0.5}$ of the as-prepared glass, we observe that K_{Ic} slightly increases (although within the error range) to 0.69 and 0.65 MPa·m$^{0.5}$ for the samples heat-treated at 648 and 790 K, respectively. The highest value of K_{Ic}, i.e., 0.73 MPa·m$^{0.5}$, is measured for the sample heat-treated at 892 K for 4 h.

Crack resistance (*CR*) refers to the ability of the glass to resist crack initiation under the impact of a sharp object. For the Vickers indentation method, it is defined as the corresponding load when the probability for corner cracking reaches 50% [11]. Fig. 6 shows the curves of crack initiation probability as a function of applied indentation load for the different samples, while the specific values of *CR* are given in Table 1. The crack resistance is generally improved upon heat treatment, especially for the temperature of 648 K, for which *CR* has increased from 5.2 to 11.2 N, i.e., an increase of more than 110% compared with the as-prepared glass. However, for higher treatment temperatures, the increase compared to the as-prepared sample is smaller. That is, *CR* is 8.7 N and 7.7 N for the glasses treated at 790 and 892 K, respectively.

3.4. Optical transparency

Fig. 7a shows photographs of the polished as-prepared and heat-treated glasses. As shown, even after heat treatment, the phase-separated glasses appear optically transparent. To quantify this observation, Fig. 7b shows the measured UV–VIS transmittance of the glasses

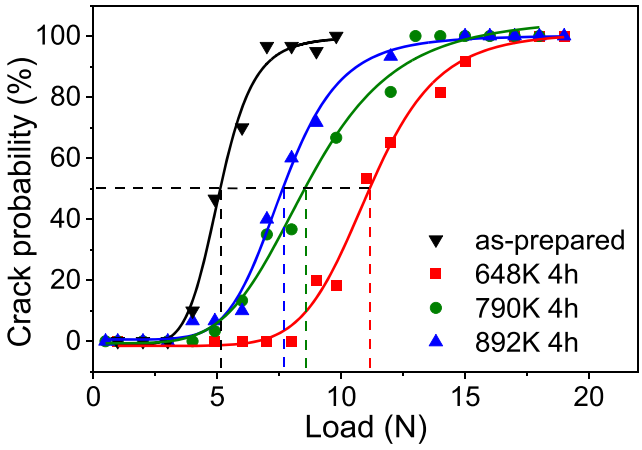

Fig. 6. Crack probability as a function of applied indentation load for the same samples.

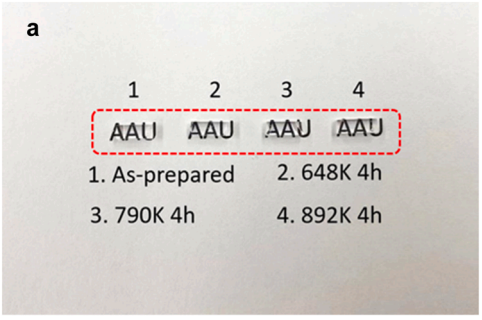

Fig. 7. (a) Photographs of polished glasses before and after heat treatments (superimposed over the AAU text). (b) UV–VIS transmittance spectra of the as-prepared and heat-treated glasses.

as a function of wavelength. There is almost no change in transmittance upon heat treatment, with very high transmittance above 90% in most of the visible region for all glass samples. In previous work on CaO-Al_2O_3-SiO_2 glasses, phase-separated nano-domains with sizes between 5 and 470 nm could be observed [21]. When the average size of the nano-domains was kept below 50 nm, it is found that the glass was transparent when viewed with the naked eye. In this work, we also ensure transparency by maintaining the size of the droplet phase between 50 and 100 nm, besides the agglomeration observed in the sample heat-treated at 892 K (Fig. 3d).

4. Discussion

The mechanical properties of glasses are determined by their structure, hence, we discuss the correlations among the glass network connectivity, phase separation microstructure, and mechanical properties. First, hardness represents the resistance to elastoplastic deformation, which is determined by glass matrix structures and any secondary phase in phase-separated glasses (or crystals as in the case of glass-ceramics) [10,22,47]. For instance, an increasing amount of non-bridging oxygen will reduce the network connectivity, which in turn leads to a decrease in hardness [5,47]. On the other hand, soft particles dispersed in a stiff glass matrix may also decrease hardness, whereas it has been shown that hardness is independent of the particle size and interparticle spacing if the volume fraction of second phase is kept constant [48]. In this work, the hardness of droplet phase (B-rich phase) is low as compared to that of the glass matrix (Si-rich phase) [20]. Considering the Raman and NMR results, the fraction of droplet phase structure (B-rich boroxol ring phase) increases upon heat treatments at 648 and 790 K, but it seems to decrease for the samples heat-treated at 892 K. Thus, from the aspect of phase separation, the reduction of the soft phase favors the improvement of hardness for the glass heat-treat at 892 K. However, the connectivity of the glass network also affects the hardness, as the discussed above. The Raman and NMR results show that the intensity of the band assigned to mixed bending and stretching vibrations of bridging oxygen and N_4 increased for all heat treatments, indicating the glass network connectivity increases after heat treatment, which contributes to the increase of hardness. Further, the finding that the average coordination number of aluminum is slightly decreased after heat treatment also means higher fraction of bridging oxygen formation. Thus, the network connectivity increases for heat-treated glasses could explain the slight increase in hardness observed herein (Table 1) [49].

Previous work has shown that crack initiation resistance is closely related to the structure of both matrix and secondary phases in a phase-separated glass [23]. For example, considering the effective way of stress dissipation under the indenter, glasses with large free volume and self-adaptive networks tend to have higher crack resistance, since energy dissipation is easy to occur during the densification process [50–52]. Indeed, different residual stresses will also affect the crack resistance of the glass, especially for composite or phase-separated glasses [22]. Based on the present structure data and micro-structure morphology from the SEM, the observed variation in *CR* can be discussed from different aspects. From a structural point of view, shear deformation will occur in borate glasses where easy-slip units such as boroxol rings exist or where trigonal to tetrahedral boron transformations occur under applied stress, which can lead to higher *CR* [52]. From the perspective of stress, nano-scale phase separation and the change of the separated phase size also play important roles. Firstly, we consider the well-known Griffith-type fracture mechanics equation, $\sigma_c = \sqrt{2E\gamma_s/\pi a}$, where σ_c is the critical stress required to create a new crack surface, a is the size of a central crack, E is the modulus of elasticity and γ_s is the fracture surface energy per unit area [53]. If the crack size around a single particle is assumed to be proportional to the size of the particle/matrix interface area, the critical debonding stress will increase as the particle size decreases [54,55]. Secondly, the nano-scale inclusions have different energy absorption mechanisms from conventional composites. As the nano-particle size decreases (at constant volume fraction of droplets), the total surface area of particle/matrix interfaces available for energy dissipation increases, meanwhile the critical stress for particle/matrix debonding also increases, which can cause the nano-separated glass to be more resistant against crack initiation [54]. Thirdly, based on finite element method calculations coupled with the mode mixity of interfacial cracks in fracture mechanics (mode mixity considering the mode I and II stress intensity factors of the interfacial crack), attempts have been made to understand the effect of the particle size (in μm-scale) on the failure process [56]. Maximum energy release rate criterion has been extensively used to predict the initiation of mixed mode cracks through calculating the energy release rate around the crack tip [57–59]. It is known that the interface characteristics are crucial for the material's mechanical response, so the energy release rate at the interface between the droplet phase (inclusion) and glass (matrix) may determine the crack behavior of transparent modifier-free glasses with phase separation. According to the maximum energy release rate criterion [58,59], the interfacial pre-existing crack for smaller particles requires higher applied stress to grow into an observable crack, because the energy release rate decreases as the particle size decreases for the same applied stress in spherical particle inclusion composite materials [56]. It should be noted that droplet phases in a transparent modifier-free glass can be regarded as inclusions inside a homogeneous/heterogeneous matrix according to the fracture mechanics, which is the same as the particle inclusion composites. As a result, the crack at the interface between the droplet phase and glass matrix requires higher applied stress to propagate.

In summary, this might at least partly explain why the crack

initiation probability decreases as the separated phase size decreases. Since the separated phase size decreases from 87 nm in the as-prepared glass to 63 and 57 nm in the glasses heat-treated at 648 and 790 K, respectively, the crack resistance has improved significantly upon heat treatment (Table 1). We also note that *CR* does not increase monotonically with the decrease of the droplet phase size, possibly because the volume fraction of the inclusion (droplet phase) is not exactly the same in the glass samples after heat treatments at 648 K and 790 K for 4 h. Therefore, the glass after heat treatment at 648 K for 4 h shows the highest *CR* owing to its highest content of separated phase (boroxol ring) with a smaller size of separated phase compared to the as-prepared glass. Although the fraction of boroxol rings in the glass after heat treatment at 790 K only slightly increases, the smallest size of droplet phase is favorable to increase *CR*. While the fraction of boroxol rings decreases after heat treatment at 892 K, which is not favorable for improving *CR*, the nano-size effect plays a more critical role in the improvement of *CR*, i.e., the *CR* of this sample also increases.

Finally, the fracture toughness is also determined by the structure and phase separation in the glass. For homogeneous glasses, K_{Ic} is sensitive to the network connectivity, since less cross-linked networks display less resistance to crack propagation on account on their lower cohesion [49,60]. For phase-separated glasses, the secondary phase droplets will either blunt or pin the crack front [23]. K_{Ic} depends on the properties of the individual particulate and matrix phases, as well as the particulate size and volume fraction. Regarding the role of the size of the separated phase, some studies have found that glasses with larger droplets phase exhibit more toughening [61,62]. Furthermore, the phase boundaries provide more discontinuities to arrest the motion of cracks, thus increasing K_{Ic} [18,63]. Thus, the observed increase of K_{Ic} herein upon heat treatment might be explained by the increase of the interface caused by the decrease of the droplet size in the glass heat-treated at 648 and 790 K (see Fig. 3). The separated phase agglomeration up to 300 nm in the glass heat-treated at 892 K results in a more significant increase in K_{Ic}. An alternative or additional explanation could be that the heat treatment makes the glass phases in the droplet and matrix more different from each other, as evidenced from the divergence of their T_g values (Fig. 2b). Indeed, peridynamics simulations have shown that the higher the stiffness mismatch between droplets and matrix in phase-separated glasses, the higher the increase in K_{Ic} [64].

In a PbO-rich matrix glass system with B_2O_3-rich particles, residual tensile stress exists within particles, as $\alpha_m < \alpha_p$ for this composite system, where α_m and α_p are the thermal expansion coefficient of the matrix and particles, respectively [62]. Therefore, the growing crack can easily penetrate the B_2O_3-rich particles. When the crack front within particles reaches the particle-matrix interface, the crack tip is assumed to be locally blunted at the interface [23]. This localized crack blunting may momentarily inhibit the extension of the entire crack front, and such impedance to crack extension becomes more effective as the volume fraction of the secondary phase particles increases. Similarly, in this work, the α_m of the Si-rich matrix is lower than the α_p of the B-rich secondary phase [65]. Therefore, compared with the as-prepared glass, more droplet phases formed in the glass heat-treated at 648 K and 790 K might also help to explain the increase in K_{Ic} in this phase-separated glass system.

5. Conclusion

In this work, we have reported a highly transparent modifier free glass (B_2O_3-SiO_2-Al_2O_3-P_2O_5) with nanoscale droplet phase separation and investigated the effects of different heat treatments on the structure and mechanical properties. Heat treatment at 648 K for 4 h (below T_{g1} of the droplet glass phase) promotes the formation of boroxol ring units, but meanwhile the droplet size decreases from 87 nm in the as-prepared glass to 63 nm. Such structural changes lead to an increase of crack resistance from 5.2 N for the as-prepared glass to 11.2 N after heat treatment. Although the heat treatments at 790 K and 892 K for 4 h do not contribute to the formation of more boroxol rings, the decreased droplet size in these two glasses also tends to improve the crack resistance, but only to around 8–9 N. For heat treatment up to 892 K (T_{g2} of the glass matrix phase), the separated phases agglomerate up to 300 nm, which contributes to the increase in fracture toughness from 0.61 $MPa{\cdot}m^{0.5}$ of the as-prepared glass to 0.73 $MPa{\cdot}m^{0.5}$ after this heat treatment. Moreover, the hardness of the glass slightly increases for all heat treatments, whereas the glass transparency is almost unaffected. As such, for this system, we vary the size and fraction of phase separation by heat treatment. The results suggest that a decrease in the size of nanoscale separation phase and increase in its fraction can help to potentially overcome the brittleness of glass, in the route toward damage-tolerant, tough, yet transparent glasses.

CRediT authorship contribution statement

Qi Zhang: Conceptualization, Investigation, Writing – original draft. **Lars R. Jensen:** Investigation, Writing – review & editing. **Randall E. Youngman:** Investigation, Formal analysis, Writing – review & editing. **Theany To:** Investigation, Writing – review & editing. **Tao Du:** Investigation, Writing – review & editing. **Mathieu Bauchy:** Conceptualization, Writing – review & editing. **Morten M. Smedskjaer:** Conceptualization, Supervision, Writing – original draft.

Declaration of Competing Interest

The authors declare that they have no known competing financial interests or personal relationships that could have appeared to influence the work reported in this paper.

Data availability

Data will be made available on request.

Acknowledgments

We thank the financial support from the European Union's Horizon 2020 Research and Innovation Program under the Marie Sklodowska-Curie Grant agreement No. 882520. MB acknowledges funding from the National Science Foundation under grant CMMI-1762292.

Supplementary materials

Supplementary material associated with this article can be found, in the online version, at doi:10.1016/j.jnoncrysol.2022.121806.

References

[1] L. Wondraczek, J.C. Mauro, J. Eckert, U. Kühn, J. Horbach, J. Deubener, T. Rouxel, Towards ultrastrong glasses, Adv. Mater. 23 (2011) 4578–4586.
[2] J.C. Mauro, A. Tandia, K.D. Vargheese, Y.Z. Mauro, M.M. Smedskjaer, Accelerating the design of functional glasses through modeling, Chem. Mater. 28 (2016) 4267–4277.
[3] T. To, L.R. Jensen, M.M. Smedskjaer, On the relation between fracture toughness and crack resistance in oxide glasses, J. Non-Cryst. Solids 534 (2020), 119946.
[4] K. Januchta, M. Bauchy, R.E. Youngman, S.J. Rzoska, M. Bockowski, M. M. Smedskjaer, Modifier field strength effects on densification behavior and mechanical properties of alkali aluminoborate glasses, Phys. Rev. Mater. 1 (2017), 063603.
[5] K.F. Frederiksen, K. Januchta, N. Mascaraque, R.E. Youngman, M. Bauchy, S. J. Rzoska, M. Bockowski, M.M. Smedskjaer, Structural compromise between high hardness and crack resistance in aluminoborate glasses, J. Phys. Chem. B 122 (2018) 6287–6295.
[6] X. Li, L. Jiang, X. Zhang, Y. Yan, Influence of residual compressive stress on nanoindentation response of ion-exchanged aluminosilicate float glass on air and tin sides, J. Non-Cryst. Solids 385 (2014) 1–8.
[7] R. Briard, C. Heitz, E. Barthel, Crack bridging mechanism for glass strengthening by organosilane water-based coatings, J. Non-Cryst. Solids 351 (2005) 323–330.

[8] J.J. Lewandowski, M. Shazly, A.S. Nouri, Intrinsic and extrinsic toughening of metallic glasses, Scr. Mater. 54 (2006) 337–341.
[9] K. Januchta, M.M. Smedskjaer, Indentation deformation in oxide glasses: quantification, structural changes, and relation to cracking, J. Non-Cryst. Solids: X 1 (2019), 100007.
[10] K. Januchta, R.E. Youngman, A. Goel, M. Bauchy, S.L. Logunov, S.J. Rzoska, M. Bockowski, L.R. Jensen, M.M. Smedskjaer, Discovery of ultra-crack-resistant oxide glasses with adaptive networks, Chem. Mater. 29 (2017) 5865–5876.
[11] P. Liu, K. Januchta, L.R. Jensen, M. Bauchy, M.M. Smedskjaer, Competitive effects of free volume, rigidity, and self-adaptivity on indentation response of silicoaluminoborate glasses, J. Am. Ceram. Soc. 103 (2020) 944–954.
[12] Z. Dong, J. Lai, W. Huang, S. Pang, H. Zhuang, H. Zhan, D. Tang, K. Chen, T. Zhang, A robust glass-ceramic sealing material for solid oxide fuel cells: effect of $Ba_3Nb_{10}O_{28}$ phase, J. Eur. Ceram. Soc. 39 (2019) 1540–1545.
[13] H. Yang, S. Wu, J. Hu, Z. Wang, R. Wang, H. He, Influence of nano-ZrO_2 additive on the bending strength and fracture toughness of fluoro-silicic mica glass–ceramics, Mater. Des. 32 (2011) 1590–1593.
[14] H. Li, D. Wang, X. Meng, C. Chen, Effect of ZrO_2 additions on the crystallization, mechanical and biological properties of MgO–CaO–SiO_2–P_2O_5–CaF_2 bioactive glass-ceramics, Colloids Surf. B 118 (2014) 226–233.
[15] H. Abdoli, P. Alizadeh, D. Boccaccini, K. Agersted, Fracture toughness of glass sealants for solid oxide fuel cell application, Mater. Lett. 115 (2014) 75–78.
[16] K.C. Jajam, H.V. Tippur, Role of inclusion stiffness and interfacial strength on dynamic matrix crack growth: an experimental study, Int. J. Solids Struct. 49 (2012) 1127–1146.
[17] D. Quesada, D. Leguillon, C. Putot, Multiple failures in or around a stiff inclusion embedded in a soft matrix under a compressive loading, Eur. J. Mech. A Solids 28 (2009) 668–679.
[18] A. Seal, P. Chakraborti, N.R. Roy, S. Mukherjee, M. Mitra, G. Das, Effect of phase separation on the fracture toughness of SiO_2-B_2O_3-Na_2O glass, Bull. Mater. Sci. 28 (2005) 457–460.
[19] G.H. Beall, L.R. Pinckney, Nanophase glass-ceramics, J. Am. Ceram. Soc. 82 (1999) 5–16.
[20] H. Liu, R.E. Youngman, S. Kapoor, L.R. Jensen, M.M. Smedskjaer, Y. Yue, Nano-phase separation and structural ordering in silica-rich mixed network former glasses, Phys. Chem. Chem. Phys. 20 (2018) 15707–15717.
[21] L. Martel, M. Allix, F. Millot, V. Sarou-Kanian, E. Véron, S. Ory, D. Massiot, M. Deschamps, Controlling the size of nanodomains in calcium aluminosilicate glasses, J. Phys. Chem. C 115 (2011) 18935–18945.
[22] O. Peitl, E.D. Zanotto, F.C. Serbena, L.L. Hench, Compositional and microstructural design of highly bioactive P_2O_5–Na_2O–CaO–SiO_2 glass-ceramics, Acta Biomater. 8 (2012) 321–332.
[23] N. Miyata, S.-i. Takeda, H. Jinno, Slow crack growth in phase-separated glasses, J. Non-Cryst. Solids 95 (1987) 1047–1054.
[24] J.F.S. Christensen, S.S. Sørensen, T. To, M. Bauchy, M.M. Smedskjaer, Toughening of soda-lime-silica glass by nanoscale phase separation: molecular dynamics study, Phys. Rev. Mater. 5 (2021).
[25] S. Cheng, C. Song, P. Ercius, Indentation cracking behaviour and structures of nanophase separation of glasses, Phys. Chem. Glasses B 58 (2017) 237–242.
[26] W.F. Du, K. Kuraoka, T. Akai, T. Yazawa, Study of Al_2O_3 effect on structural change and phase separation in Na_2O-B_2O_3-SiO_2 glass by NMR, J. Mater. Sci. 35 (2000) 4865–4871.
[27] S. Morimoto, Phase separation and crystallization in the system SiO_2–Al_2O_3–P_2O_5–B_2O_3–Na_2O glasses, J. Non-Cryst. Solids 352 (2006) 756–760.
[28] A. Mazzoli, O. Favoni, Particle size, size distribution and morphological evaluation of airborne dust particles of diverse woods by scanning electron microscopy and image processing program, Powder Technol. 225 (2012) 65–71.
[29] K. Kapat, P.K. Srivas, A.P. Rameshbabu, P.P. Maity, S. Jana, J. Dutta, P. Majumdar, D. Chakrabarti, S. Dhara, Influence of porosity and pore-size distribution in Ti6Al4 V foam on physicomechanical properties, osteogenesis, and quantitative validation of bone ingrowth by micro-computed tomography, ACS Appl. Mater. Interfaces 9 (2017) 39235–39248.
[30] M. Ender, J. Joos, T. Carraro, E. Ivers-Tiffée, Quantitative characterization of $LiFePO_4$ cathodes reconstructed by FIB/SEM tomography, J. Electrochem. Soc. 159 (2012) A972.
[31] D. Massiot, F. Fayon, M. Capron, I. King, S. Le Calvé, B. Alonso, J.O. Durand, B. Bujoli, Z. Gan, G. Hoatson, Modelling one-and two-dimensional solid-state NMR spectra, Magn. Reson. Chem. 40 (2002) 70–76.
[32] D. Neuville, L. Cormier, D. Massiot, Role of aluminium in peraluminous region in the CAS system, Geochim. Cosmochim. Acta 68 (2004) 5071–5079.
[33] P. Liu, R.E. Youngman, L.R. Jensen, M. Bockowski, M.M. Smedskjaer, Achieving ultrahigh crack resistance in glass through humid aging, Phys. Rev. Mater. 4 (2020), 063606.
[34] M. Wada, H. Furukawa, K. Fujita, Crack resistance of glass on Vickers indentation, Proc. Int. Congr. Glass 11 (1974) 39–46.
[35] T. To, S.S. Sørensen, J.F. Christensen, R. Christensen, L.R. Jensen, M. Bockowski, M. Bauchy, M.M. Smedskjaer, Bond switching in densified oxide glass enables record-high fracture toughness, ACS Appl. Mater. Interfaces 13 (2021) 17753–17765.
[36] T. To, S.S. Sørensen, M. Stepniewska, A. Qiao, L.R. Jensen, M. Bauchy, Y. Yue, M. M. Smedskjaer, Fracture toughness of a metal–organic framework glass, Nat. Commun. 11 (2020) 1–9.
[37] T. To, F. Célarié, C. Roux-Langlois, A. Bazin, Y. Gueguen, H. Orain, M. Le Fur, V. Burgaud, T. Rouxel, Fracture toughness, fracture energy and slow crack growth of glass as investigated by the Single-Edge Precracked Beam (SEPB) and Chevron-Notched Beam (CNB) methods, Acta Mater. 146 (2018) 1–11.
[38] Z. Raheem, Standard test methods for determination of fracture toughness of advanced ceramics at ambient temperature, Ceram. Mater. (2010). ASTM International.
[39] H. Gan, P. Hess, R. Kirkpatrick, Phosphate and boron speciation in K_2O–B_2O–SiO_2–P_2O_5 glasses, Geochim. Cosmochim. Acta 58 (1994) 4633–4647.
[40] H. Liu, M.M. Smedskjaer, H. Tao, L.R. Jensen, X. Zhao, Y. Yue, A medium range order structural connection to the configurational heat capacity of borate–silicate mixed glasses, PCCP 18 (2016) 10887–10895.
[41] L. Koudelka, P. Mosner, Borophosphate glasses of the ZnO–B_2O_3–P_2O_5 system, Mater. Lett. 42 (2000) 194–199.
[42] A. Winterstein-Beckmann, D. Möncke, D. Palles, E. Kamitsos, L. Wondraczek, A Raman-spectroscopic study of indentation-induced structural changes in technical alkali-borosilicate glasses with varying silicate network connectivity, J. Non-Cryst. Solids 405 (2014) 196–206.
[43] H. Li, Y. Su, L. Li, D.M. Strachan, Raman spectroscopic study of gadolinium (III) in sodium-aluminoborosilicate glasses, J. Non-Cryst. Solids 292 (2001) 167–176.
[44] P. Liu, A.L. Søndergaard, R.E. Youngman, S.J. Rzoska, M. Bockowski, L.R. Jensen, M.M. Smedskjaer, Structural densification of lithium phosphoaluminoborate glasses, J. Am. Ceram. Soc. 104 (2021) 1345–1359.
[45] K.J. MacKenzie, M.E. Smith, Multinuclear Solid-State Nuclear Magnetic Resonance of Inorganic Materials, Elsevier, 2002.
[46] A. Kumar, S. Rai, D. Rai, Effect of thermal neutron irradiation on Gd^{3+} ions doped in oxyfluoroborate glass: an infra-red study, Mater. Res. Bull. 38 (2003) 333–339.
[47] M. Barlet, J.M. Delaye, T. Charpentier, M. Gennisson, D. Bonamy, T. Rouxel, C. L. Rountree, Hardness and toughness of sodium borosilicate glasses via Vickers's indentations, J. Non-Cryst. Solids 417 (2015) 66–79.
[48] N. Miyata, H. Jinno, Micromechanics approach to the indentation hardness of glass matrix particulate composites, J. Mater. Sci. 17 (1982) 547–557.
[49] K. Januchta, T. To, M.S. Bødker, T. Rouxel, M.M. Smedskjaer, Elasticity, hardness, and fracture toughness of sodium aluminoborosilicate glasses, J. Am. Ceram. Soc. 102 (2019) 4520–4537.
[50] X. Ke, Z. Shan, Z. Li, Y. Tao, Y. Yue, H. Tao, Toward hard and highly crack resistant magnesium aluminosilicate glasses and transparent glass-ceramics, J. Am. Ceram. Soc. 103 (2020) 3600–3609.
[51] Y. Kato, H. Yamazaki, S. Yoshida, J. Matsuoka, Effect of densification on crack initiation under Vickers indentation test, J. Non-Cryst. Solids 356 (2010) 1768–1773.
[52] G.A. Rosales-Sosa, A. Masuno, Y. Higo, H. Inoue, Crack-resistant Al_2O_3–SiO_2 glasses, Sci. Rep. 6 (2016) 1–7.
[53] L. Sun, R.F. Gibson, F. Gordaninejad, J. Suhr, Energy absorption capability of nanocomposites: a review, Compos. Sci. Technol. 69 (2009) 2392–2409.
[54] J.K. Chen, Z.P. Huang, J. Zhu, Size effect of particles on the damage dissipation in nanocomposites, Compos. Sci. Technol. 67 (2007) 2990–2996.
[55] J.K. Chen, M. Yuan, Decoupling of viscous dissipation and damage dissipation in particulate-reinforced polymeric materials, Comput. Mater. Sci. 40 (2007) 267–274.
[56] J. Cho, M. Joshi, C. Sun, Effect of inclusion size on mechanical properties of polymeric composites with micro and nano particles, Compos. Sci. Technol. 66 (2006) 1941–1952.
[57] M. Hussain, S. Pu, J. Underwood, Strain energy release rate for a crack under combined mode I and mode II, in: Fracture Analysis: Proceedings of the 1973 National Symposium on Fracture Mechanics, Part II, ASTM International, 1974.
[58] R. Nuismer, An energy release rate criterion for mixed mode fracture, Int.J. Fract. 11 (1975) 245–250.
[59] C. Wu, Fracture under combined loads by maximum-energy-release-rate criterion, J. Appl. Mech. 45 (1978) 553–558.
[60] R.J. Eagan, J. Swearekgen, Effect of composition on the mechanical properties of aluminosilicate and borosilicate glasses, J. Am. Ceram. Soc. 61 (1978) 27–30.
[61] J. Deubener, M. Höland, W. Höland, N. Janakiraman, V. Rheinberger, Crack tip fracture toughness of base glasses for dental restoration glass-ceramics using crack opening displacements, J. Mech. Behav. Biomed. Mater. 4 (2011) 1291–1298.
[62] N. Shinkai, R. Bradt, G.E. Rindone, The KIc to E relationship in phase separated glasses, J. Non-Cryst. Solids 49 (1982) 497–506.
[63] C.J. Simmons, S.W. Freiman, Effects of phase separation on crack growth in borosilicate glass, J. Non-Cryst. Solids 38 (1980) 503–508.
[64] L. Tang, N.A. Krishnan, J. Berjikian, J. Rivera, M.M. Smedskjaer, J.C. Mauro, W. Zhou, M. Bauchy, Effect of nanoscale phase separation on the fracture behavior of glasses: toward tough, yet transparent glasses, Phys. Rev. Mater. 2 (2018), 113602.
[65] M. Bengisu, Borate glasses for scientific and industrial applications: a review, J. Mater. Sci. 51 (2016) 2199–2242.